# Viscous Drag Reduction of a Nose Body

Promode R. Bandyopadhyay*
*NASA Langley Research Center, Hampton, Virginia*

**The convex curvature concept of viscous drag reduction has been applied to an axisymmetric nose-body combination. The work is described in two parts. A modified mixing-length formulation is first qualified in several complex turbulent boundary layers that are primarily curved. This is then used to design an axisymmetric nose that incorporates several recently proposed concepts of viscous drag reduction. Primarily, application is made of the fact that compared to a flat surface, the effect of streamwise convex curvature is to reduce skin friction, and the level remains lower even after the curvature is removed. A parametric study has been conducted to incorporate the conflicting requirements in a nose, viz., the application of the drag reduction concepts at an optimized level while causing no separation. The axial distribution of the cross-sectional area ratio is found to be critical to separation. This required the drag reduction concepts to be implemented over several short fetches of curvature instead of a single long fetch. A novel three-stage nose has been designed that does not separate while incorporating the drag reduction concepts. This has been compared with two "equivalent" nose bodies.**

## Nomenclature

$a,b$ = semimajor and semiminor axes of an ellipse, respectively
$A$ = surface area
$A^+$ = damping factor for zero pressure gradient flow in wall-layer variables
$c_f$ = skin friction coefficient, $\tau_w/(1/2)\rho U_e^2$
$C_d$ = drag coefficient, $D/(1/2\rho_{\text{ref}}U_{\text{ref}}^2 S)$ or $D/(1/2\rho_{\text{ref}}U_{\text{ref}}^2 V^{2/3})$
$C_P$ = coefficient of pressure, $(P-P_{\text{ref}})/(1/2\rho_{\text{ref}}U_{\text{ref}}^2)$
$d$ = main cylinder (body) diameter
$D$ = drag
$f$ = primary lag variable, $A^+$, $K$ or $R$
$F$ = function in Bradshaw's buoyancy analogy of curvature effect
$h$ = heat-transfer coefficient
$H$ = form factor, $\delta^*/\theta$
$K$ = Prandtl constant describing slope of mixing length near wall
$\ell$ = mixing length
$L$ = lag constant
$L_s$ = length of a body of revolution measured along surface
$M$ = Mach number
$P$ = pressure
$P^+$ = pressure gradient, $(\nu/\rho U_\tau^3)(dP_w/ds)$
$R$ = radius of longitudinal curvature
$Re_s$ = surface length Reynolds number, $U_e s/\nu$
$Re_\theta$ = momentum thickness Reynolds number, $U_e\theta/\nu$
$S$ = surface area
$s,y$ = coordinates along and normal to the surface
$s_c$ = distance along surface measured from end of concave region
$s^*$ = nondimensional distance along body surface in streamwise direction measured from nose stagnation point, $s/L_s$
$U$ = velocities within the boundary layer in the $s$-direction
$U_\tau$ = friction velocity
$V$ = volume
$x$ = axial distance from nose in axisymmetric bodies
$\alpha$ = Bradshaw constant in buoyancy analogy of curvature effect
$\beta$ = pressure gradient parameter, $(\delta^*/\tau_w)(dP_w/ds)$
$\delta$ = boundary-layer thickness: value of $y$ corresponding to $U/U_e = 0.995$
$\delta_i$ = $\delta$ at the start of a flat length following the end of a curved region
$\delta^*$ = displacement thickness, $\int_0^\infty(1-U/U_e)\,dy$
$\Delta s$ = total length of a continuously curved surface
$\theta$ = nomentum thickness, $\int_0^\infty U/U_e(1-U/U_e)\,dy$
$\tau_w$ = wall shear stress
$\nu$ = kinematic viscosity
$\phi$ = turning angle in a concave or convex region

*Subscripts*

$e$ = boundary-layer edge value
eff = local effective value
eq = equilibrium value
ref = reference or nominal oncoming flow condition
$w$ = wall value

Presented as Paper 88-0135 at the AIAA 26th Aerospace Sciences Meeting, Reno, NV, Jan. 11-14, 1988; received March 21, 1988; revision received June 27, 1988. 

*Senior Research Associate. Associate Fellow AIAA.

## I. Introduction

PRANDTL'S early works show that a streamwise convex surface curvature has a stabilizing effect on boundary layers. A marked effect of this on turbulent boundary layers is to lower wall shear stress below what would occur in a flat surface at the same Reynolds number. Recent experiments[1-3] show that when curvature ratio is large ($\delta/R > 0.05$), wall shear stress remains low over a streamwise distance of many $\delta$ even after the curvature is removed. Bushnell[4] has proposed that this effect of convex surface curvature be incorporated into axisymmetric bodies to see if the viscous component of drag is reduced. This will be referred to as the convex curvature concept of viscous drag reduction. The present work is the first contribution toward the implementation of this concept.

## II. Computation of Curved Boundary Layers

A literature survey shows that modeling of curved flows is difficult because the physics of the flow is not well understood. In the present work, it is assumed that the usual boundary-layer assumptions apply to flow over curved surfaces. The purpose of this part of the work has been to modify an existing boundary-layer code appropriately and qualify it in a variety of complex turbulent boundary layers that are pri-

marily curved. It is desirable that, first, the code be successfully tested in all complex strains anticipated in the low viscous drag axisymmetric nose body to be designed in the second part of this work.

### A. Choice of Mixing-Length Model

The two foundations of the turbulence modeling used in the present work are Prandtl's mixing-length and Bradshaw's[5] buoyancy analogy of the effect of streamline curvature. Saffman[6] has critically examined various theoretical approaches to study turbulence and has listed construction of scaling laws or physical models as the most intelligible and relevant to real turbulence problems. Analogy is a tool of model construction, and he explicitly cites the above two analogies as examples of what a physical model should be. Mixing-length models have been extensively studied and used in aeronautical problems, and an evaluation has been given by Galbraith and Head[7]—a work that in Schlichting's[8] words provides "good experimental support for the utility of the mixing-length concept."

There are other associated reasons for the present choice of a mixing-length approach. Other turbulence models like the standard $k$-$\epsilon$ or variations of it, which attempt to take into account more details of the transport process, would be an alternative; however, in curved flows, these are still known to overpredict the turbulent shear stress in a convex wall, and underpredict in a concave wall.[9] An area of particular interest to the present drag reduction work is the region of recovery following a long fetch of high-curvature ratio ($\delta/R > 0.05$). Gillis and Johnston[2] and Alving and Smits[3] have performed the relevant experiments. This recovery region is a challenge to modeling and so far, Adams and Johnston's[10] empirical mixing-length work is the only attempt to compute this type of flow. If any model had existed today that could handle the recovery region successfully, then it would, of course, be a good candidate for the present work. In the concave wall, all turbulence models come to grief because they are unable to predict or deal with the periodic three-dimensional flow over the span created by the formation of stationary turbulent Taylor-Goertler vortices.[11]

Another contributing factor is that the experience with mixing-length models in wavy walls, whose alternating pressure gradients are very similar to those in the axisymmetric configurations studied here in the second part, are well documented.[12] An attractive feature of their modeling has been the simplicity and ease with which separately identifiable strains and their lag rates can be turned on or off. Like that work, the premise in the present also has been that the absolute drag levels computed may perhaps be somewhat in error, but the trends are generally correct. Finally, the purpose of the present work is not to evaluate turbulence models in curved flows per se, but to use a well-understood engineering tool to see if the design of an axisymmetric low viscous drag nose body is feasible.

### B. Method

The basic code (VGBLP) used to compute the boundary layers is that written by Harris and Blanchard.[13] The governing equations are solved by an implicit finite-difference procedure. A mixing-length model is used for turbulence closure. This allowed several additional effects, discussed below, to be added in a simple manner. Note that transverse curvature effect that leads to a thinning of boundary layer was already coded by the originators.

Cary et al.[12] have used a mixing-length model where a number of complex strain effects are separately incorporated to compute boundary layers over wavy walls. These are 1) effect of pressure gradient on effective viscous sublayer thickness $A^+$, 2) the lag in the response of $A^+$ to rapid changes in pressure gradient $P^+$, 3) effect of pressure gradient on Prandtl constant $K$ that describes the slope of mixing length near wall, 4) the lag in the response of $K$ to $P^+$, 5) effect of longitudinal surface curvature on mixing length, and 6) the lag in the response of mixing length to curvature. The curvature effect is incorporated as per Bradshaw's[5] Richardson number formulation. Here, the flat plate equilibrium mixing length $\ell_{eq}$ is adjusted for curvature effects to obtain its effective value $\ell_{eff}$:

$$\ell_{eff} = F \cdot \ell_{eq} \tag{1}$$

where $F = 1 - \alpha(2U/R)/(\partial U/\partial y)$. Here, $U$ is surface-parallel velocity, $y$ is surface-normal distance, and $\alpha$ is a constant whose value is allowed to vary between convex and concave surfaces in view of the asymmetric response of boundary layers to curvature.[14]

All three lag equations are similar in form:

$$\frac{d}{ds}\left(\frac{1}{f_{eff}}\right) = \frac{1}{L_f}\left(\frac{1}{f_{eq}} - \frac{1}{f_{eff}}\right) \tag{2}$$

Here, $f$ is the primary lag variable, viz., $A^+$, $K$, or $R$, and the subscripts are defined with Eq. (1). The streamwise surface distance is $s$, and $L$ is the particular lag constant. In a curvature study, lag is considered by substituting $R_{eff}$ for $R$ in the form of $F$ in Eq. (1). The above effects were earlier coded into VGBLP by Eidson,[15] but they remained to be verified.

To verify the code and determine the constants in the model equations of extra effects, 14 experimental flowfields have been chosen that are primarily curved. Most of the results of these computations are given in the next subsection.

A careful reading of Cary et al.'s[12] work shows that their wavy wall is dominated by pressure effects and not surface curvature effects. Additionally, there the lag effects 2 and 4 are important because pressure changes between large $\beta$ limits (near-relaminarization and separation) over relatively short streamwise distances compared to $\delta$. Thus, the wavy wall has a basic difference from the test cases of curved flows under consideration.

In the present computations of the test cases, effects 2–4 have been ignored completely, the justification being that, unlike that in a wavy wall, the pressure gradients are not so severe, and they do not change rapidly. The reasonable agreement found later between the computed and measured $c_f$, $\theta$, and $H$ values confirmed this supposition. What disagreement is there can plausibly be ascribed partly to a lack of two-dimensionality in the experimental flowfields. Effects 1 and 5 always have been considered: since the existence of effect 1 is beyond dispute, it has been considered whenever pressure gradient is present in any part of the flow—the detailed measured pressure gradient always has been input (curvature is assumed to have no effect on $A^+$). Similarly, effect 5 always has been considered in the curved regions of the flows: $\alpha$ is 7.0 in all convex surfaces and lower (3.0 or 5.0) in concave surfaces. Effect 6 always has been ignored in two-dimensional concave surfaces; however, it is always considered in two-dimensional convex surfaces when streamwise pressure gradient is present at the curvature junction. The aforementioned guidelines for considering the extra effects are well defined. The other constants used in the computations, but not mentioned here, are given in Harris and Blanchard,[13] and they have not been changed from one flow to another.

### C. Results

The streamwise development of the computed boundary-layer integral quantities, viz., $c_f$, $H$, and $Re_\theta$, have been compared against measurements in Figs. 1–11 and Fig. 18 out of which the convex surface results are given in Figs. 1–6 and Fig. 18.

The two-dimensional convex geometry of Smits et al.,[1] considered in Fig. 1, has streamwise favorable and adverse pressure gradients over the curved surface which have been included in the computations. Although the curvature ratio $\delta/R$ is high (0.1) here, the fetch of curvature is short ($\Delta s/\delta_i = 3$). Consequently, the flow shows a relatively quick recovery[14] (cf. Fig. 2).

The two-dimensional geometry of Gillis and Johnston,[2] considered in Fig. 2, had a streamwise pressure gradient that was carefully set to zero by means of external flow controls. The curvature ratio $\delta/R$ and the curved length ratio $\Delta s/\delta_i$ were large (0.05–0.10 and 15–31, respectively). This experiment first demonstrated that a high ratio and a long fetch of convex curvature lead to a very slow $c_f$ recovery [0(100$\delta$)]. The relaxation has been modeled assuming that the streamlines lose their curvature gradually after such a convex turn. Based on the experiments, the computed distributions have been obtained assuming a 110$\delta$ length of recovery. Thus, from the end of the convex region, the effective $\delta/R$, in mixing-length computation only, is simply assumed to drop linearly to 0.01 over this length. The above $\delta/R$ cutoff value for curvature effect is based on the mixing-length computations of Adams and Johnston.[10]

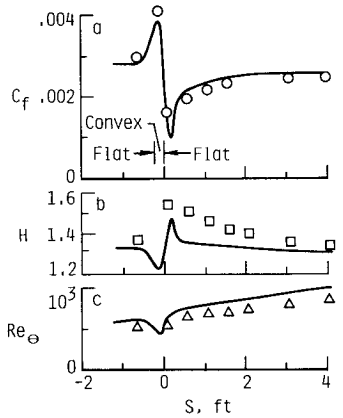


**Fig. 1 Computations compared with measurements[1] in a two-dimensional flat wall boundary layer recovering after a 30 deg convex turn, $U_{ref}$ = 105 fps. In all figures, unless stated otherwise, lines and symbols represent computations and measurements, respectively.**

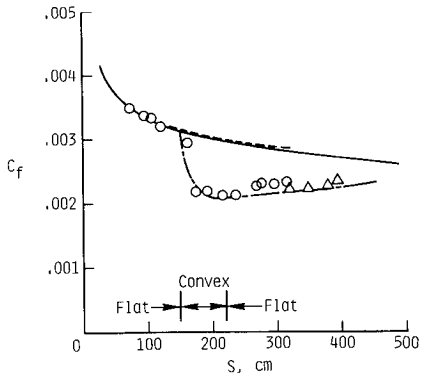


**Fig. 2 Computed $c_f$ compared with measurements[2] in a two-dimensional flat wall boundary layer recovering after a 90 deg convex turn; triangles are from Ref. 18; $U_{ref}$ = 15 m/s; nominal $dP/ds = 0$. Computations: chain line—curved flow; solid line—flat wall; uniformly broken line compares STAN5 flat wall code[2] with present computations (solid line).**

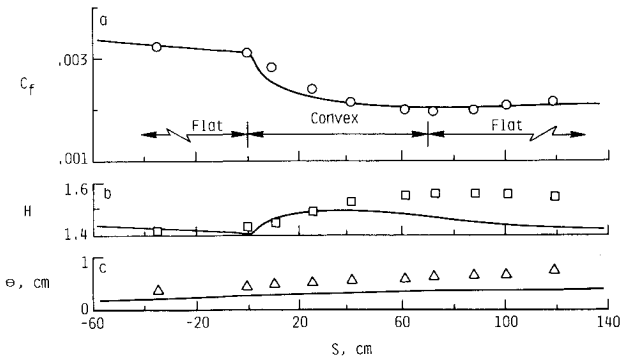


**Fig. 3 Computed developments compared with measurements[16], run 070280 taken in the same facility as in Fig. 2; $U_{ref}$ = 15 m/s.**

In Fig. 3, boundary-layer computations for the Gillis and Johnston[2] geometry considered in Fig. 2 above are compared with the more detailed measurements of Simon et al.[16] As before, a 110$\delta$ recovery length is assumed in the computations.

In Fig. 4 also, the flow geometry is the same as that of Gillis and Johnston[2] (Fig. 2), except that the recovery was measured by Alving and Smits[3] over a larger length. As in Figs. 2 and 3, the computations are based on a zero streamwise pressure gradient and a 110$\delta$ recovery length. However, this flow had a slight streamwise pressure gradient at the curvature junctions that was taken into account through a lag in the curvature effect (Sec. IIB).

In the flow of Muck et al.,[17] considered in Fig. 5, both the curvature ratio ($\delta/R \approx 0.01$) and pressure gradients are mild. On the other hand, both these quantities are much higher ($\delta/R \approx 0.1$ and separating) in the So and Mellor[19] flow considered in Fig. 6, which is also known to be a difficult flow to compute. Figure 6 shows that the curvature effect on skin friction in the presence of an adverse pressure gradient, which is given by the difference between the solid and broken lines, remains clearly large.

The results of the concave surface computations are given in Figs. 7–11. In the flow of Smits et al.,[1] shown in Fig. 7, as in its convex counterpart in Fig. 1, the concave curvature ratio $\delta/R$ is large (0.1), and the curved length ratio $\Delta s/\delta_i$ is small (5). The $\delta/R$ level is clearly large enough to produce a standing

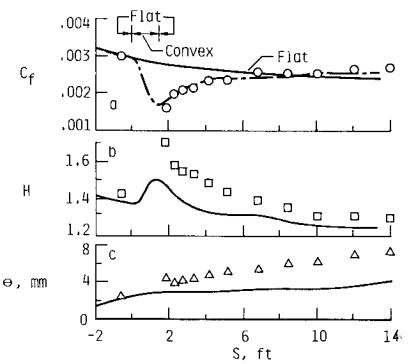


**Fig. 4 Computations compared with measurements[3] in a flow geometry similar to that in Fig. 2, $U_{ref}$ = 23.4 m/s. In a: chain line—curved; solid line—flat surface.**

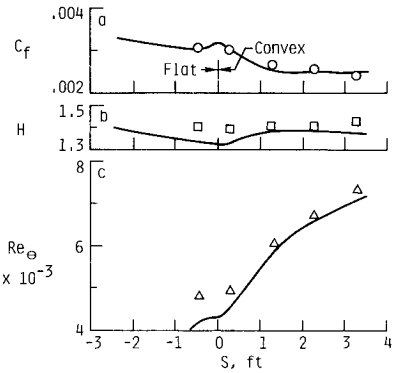


**Fig. 5 Computations compared with measurements[17] in a two-dimensional flat wall followed by a long fetch of mild convex curvature, $U_{ref}$ = 33 m/s.**

spanwise array of turbulent Taylor-Goertler vortices. The flow geometry has favorable and adverse pressure gradients in the curved region, which have been included in the computations. The crest and trough (defined as high- and low-$c_f$ regions, respectively) measurements have been computed separately assuming two-dimensional flows, but with $\alpha$ varying from 5.0-3.0, respectively.

The Shizawa and Honami[20] concave flow computations shown in Fig. 8 were also carried out assuming a two-dimensional flow and an $\alpha$ of 5.0. The measurements are probably for a halfway station between crests and troughs. The flow

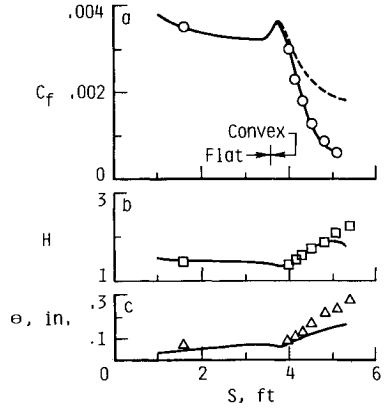


**Fig. 6 Computations compared with measurements[19] in a two-dimensional flat wall followed by a long fetch of convex surface with increasing radius of curvature; $dP/ds$ in the convex region is adverse; $U_{ref}$ = 71 fps. Solid and broken lines: computations with and without curvature effects, respectively.**

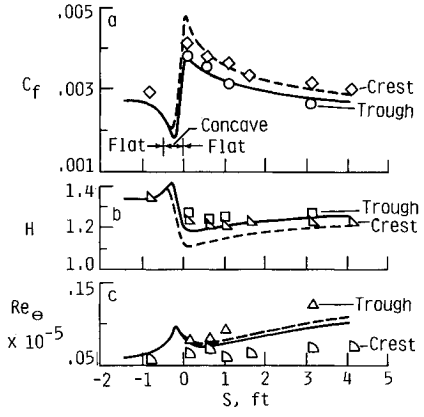


**Fig. 7 Computations compared with measurements[1] in a two-dimensional flat wall boundary layer recovering after a 30 deg concave turn, $U_{ref}$ = 105 fps, $\alpha$ = 3 (solid line) and 5 (broken line).**

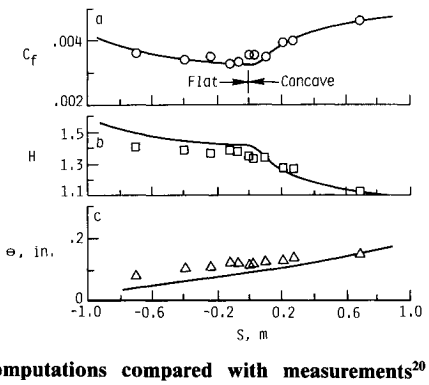


**Fig. 8 Computations compared with measurements[20] in a two-dimensional flat wall followed by a concave region of constant curvature, nominal $dP/ds$ = 0, $U_{ref}$ = 15 m/s.**

geometry has no relaxation length but, in view of the high values of $\delta/R$ (0.05) and $\Delta s/\delta$ (50), it is a concave counterpart of Gillis' and Johnston's[2] convex curvature experiment presented in Fig. 2. However, unlike all other two-dimensional concave-surface experiments (Figs. 7, 9, and 10), streamwise pressure gradient was largely removed here by contouring the opposite wall, and the indirect evidence is that the Taylor-Goertler vortices are weaker and irregularly spaced compared to the equally high $\delta/R$ case of Fig. 7 above. This might explain the slightly better agreement in Fig. 8 than in Fig. 7.

The flow of Hoffmann et al.,[21] shown in Fig. 9, has a weak curvature ratio $\delta/R$ of 0.01-0.02. The measurements shown are from the earlier companion work of Hoffmann and Bradshaw.[22] The measured mild pressure gradient has been included in the computations, which have been carried out for $\alpha$ = 5.0 and assuming a two-dimensional flow. The measurements of Hoffmann et al.[21] show that practically $H$ does not vary between the crests and troughs, which might explain the better agreement than that in the strong $\delta/R$ case shown in Fig. 7.

Figure 10 shows the results for an 8 deg compression with concave curvature. The measurements are from model 1 of Taylor and Smits.[23] Note that the drop in $c_f$ has been successfully modeled. The curvature ratio $\delta/R$ is strong (0.1) here. But, the experimenters did not observe any Taylor-Goertler roll cells, apparently due to a bulk compression behavior that is analogous to lateral divergence. This is further discussed in Sec. IIIA.

The computations and measurements shown in Fig. 11 are for the axisymmetric cylinder-flare body of Smits et al.[24] The measured surface pressure distribution in the vicinity of the concave region of this body is alternating and has been included in the computations shown in Fig. 11 (see Figs. 1 and 3 of Ref. 24). Computed inviscid pressure distributions were used in the nose region. A sudden enlargement due to the

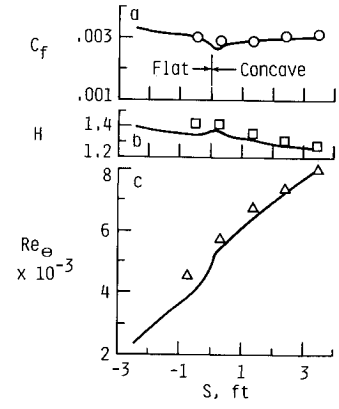


**Fig. 9 Computations compared with measurements[21] in a two-dimensional flat wall followed by a long fetch of mild concave curvature, $U_{ref}$ = 33 m/s.**

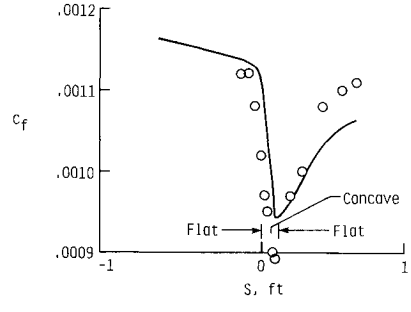


**Fig. 10 Computed $c_f$ compared with measurements[23] in a two-dimensional concave geometry, $M_{ref}$ = 2.87.**

termination of the test-section wall in their experiment created a dip in the $C_P$ distribution. Such a test-section wall is, of course, absent in the nose bodies considered in the second part. But, this alternating pressure distribution, among other features of this flow, is very similar to the complications present in the low-viscous-drag nose bodies considered later. Although the curvature ratio $\delta/R$ is high (0.08) in the concave region, the flow is uniform azimuthally, and no Taylor-Goertler vortex has been observed by the experimenters due to the presence of lateral divergence. This partly explains the good agreement between the boundary-layer computations and measurements shown in Fig. 11. The computation has been done for $\alpha = 3.0$.

## III. Viscous Drag Reduction of a Nose-Body Combination

### A. Viscous Drag Reduction Concepts

It is instructive to isolate the positive effects that can be used for viscous drag reduction purposes. But usually while applying these, some drag penalties cannot be avoided. Thus, it is also important to know how the negative effects can be simultaneously kept to a minimum. The following is a discussion of these two types of effects.

As stated earlier, the primary viscous drag reduction concept that has motivated the present work is the effect due to a convex surface curvature. This acts instantaneously. The beneficial effect persists over a limited extent even after the curvature is removed. When the curvature ratio and the fetch are large ($\delta/R > 0.05$ and $\Delta s/\delta_i > 20$) (Ref. 14), the effect may last as long as $100\delta$ or even beyond.[2,3]

Apart from the convex curvature, there are three other effects that can be simultaneously utilized to enhance the viscous drag reduction. These are adverse pressure gradients, the combined effect of lateral divergence and convex curvature, and high Reynolds number. The utilization of the first two effects are inherently connected to the fact that in the present work, the viscous drag reduction concepts are being applied to the nose of the main cylinder, i.e., where the body diameter is increasing axially. The positive effect due to adverse pressure gradient can be better utilized by contriving it to appear in a larger diameter region of the nose. This will become obvious in the following two subsections by comparing the single stage and multistage nose bodies. In the former, the forecylinder, where the adverse pressure gradient occurs, is significantly thinner.

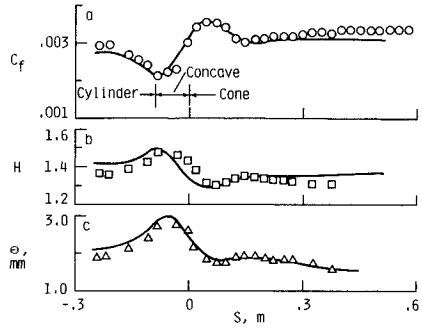


**Fig. 11 Computations compared with measurements[24] in flow along an axisymmetric cylinder-flare body having an alternating surface pressure distribution in the vicinity of the concave region, $U_{ref}$ = 38 m/s.**

The work of Smits and Joubert[25] (also see Ref. 26) shows that in a body of revolution, the viscous drag-reducing behavior of a convex curvature can be enhanced by combining it with streamline divergence over the nose. The effect of the combined strain rates is favorable, although applied singly streamline divergence is known to be destabilizing.

The last effect, that due to Reynolds number, concerns the result that in a given developing flow, wall shear stress drops as $Re_s$ increases. As in the adverse pressure gradient case, this effect can be utilized by distributing the surface area judiciously so that the high wall shear stress due to low Reynolds numbers occurs in the small diameter part of the nose.

The incorporation of a convex region in the nose body requires it to be preceded by a fetch of concave curvature, which is known to have a destabilizing effect on the boundary layer. The specific considerations given to the design of the low-viscous-drag body to deal with the concave region are discussed in the next subsection. Here, this aspect will be examined in relation to the general effect of lateral divergence and compressibility. Information on the formation of stationary Taylor-Goertler-like (turbulent) roll cells in axisymmetric concave surfaces is scant, and one assumes the nature of their formation and growth on two-dimensional surfaces to hold for bodies of revolution also. However, recent experiments surprisingly show that this is not the case, perhaps due to the simultaneous and inherent presence of at least another strain, lateral divergence. In their axisymmetric concave curvature experiment, Smits et al.[24] have observed that "In startling contrast to Smits et al.,[1] where concave streamline curvature in nominally two-dimensional flow led to development of strong spanwise variations, plausibly ascribable to longitudinal vortices, streamline curvature accompanied by lateral divergence seems if anything to reduce pre-existing circumferential variations." Therefore, in the context of viscous drag reduction of a nose body, lateral divergence has a beneficial role in both the convex and concave regions.

It appears that the suppression of Taylor-Goertler-like (turbulent) roll cells by lateral divergence can be further enhanced by the effect of bulk compression. On qualitative grounds,

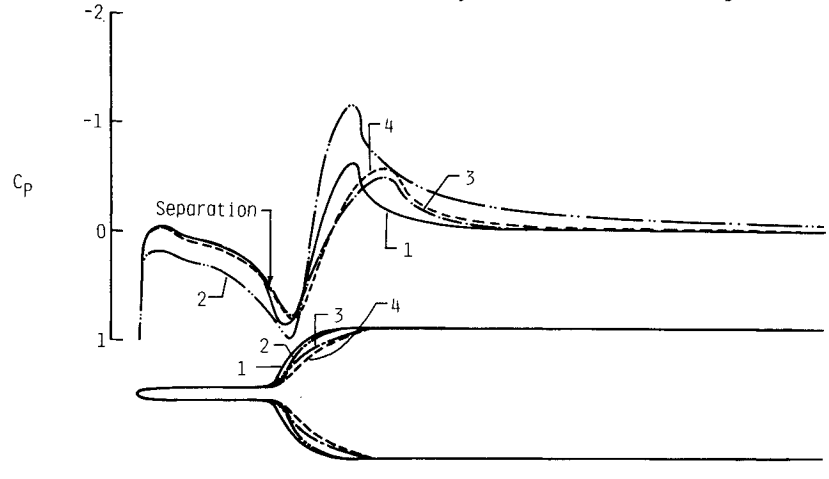


**Fig. 12 Computed surface-pressure distributions in single-stage nose geometries with straight cylindrical forebodies. Computed separation location in all four geometries is indicated, $M_{ref} = 0.5$.**

Green (see Ref. 5) has suggested that the effect of bulk compression is analogous to lateral divergence. An experimental support of this is provided by Taylor and Smits,[23] who performed experiments in a compressible turbulent boundary layer subjected to a short region of concave curvature and an adverse pressure gradient. The flow remained two-dimensional, and no Taylor-Goertler-like roll cells were observed. They concluded that "The behavior of the mean flow under the action of concave curvature and bulk compression is similar to that observed under the action of concave curvature and lateral divergence." Understandably, it needs to be confirmed that in an axisymmetric concave body, lateral divergence and bulk compression act in an additive manner in the suppression of Taylor-Goertler-like (turbulent) roll cells. Nevertheless, in the present design work discussed in the next subsection, care has been taken to minimize the chance of formation of these roll cells in the concave region.

Finally, note that the effect of transverse surface curvature in straight cylinders is to increase skin friction. However, this effect is not significant in the present work because the viscous drag reduction concepts are being applied in the nose and not in the tail of the main cylinder, wherein the ratio of boundary-layer thickness to the local body diameter remains very low. Nevertheless, in the present computations this effect has been included.

### B. Early Experience with Single-Stage Nose Bodies and Separation

Figure 12 shows a straightforward application of Bushnell's[4] concept to a cylindrical body. The following salient features of the nose body are to be noted: 1) the purpose of the small-diameter forebody is to grow a turbulent boundary layer that can "absorb" the viscous drag-reducing feature of the convex curvature that follows. The dimensions of the forebody, its diameter and length, should be small to keep its drag low; 2) the unavoidable concave region between the forebody and the convex region should be short for the following reasons: a) to avoid growth of Taylor-Goertler-like roll cells, b) to reduce integrated turbulence amplification, and c) to utilize the asymmetric effect of a convex vs a concave surface curvature; 3) the surface length of the convex region in terms of $\delta$ should be as large as possible, and $\delta/R$ on the convex surface should be $>0.05$. (Analysis of available convex curvature data shows that an asymptotic state is reached for $\delta/R>0.05$, and relaxation is slower with increase in $\Delta s/\delta$) (Ref. 14); 4) as per the concept, the levels of wall shear stress at the shoulder will now be lower than the equilibrium levels, and a viscous drag reduction can be expected due to the relaxation of the flow over the main cylinder.

The above is a single-stage nose body. Its surface pressure distribution is also shown in Fig. 12. All nose-body computations have been performed at $M_{\text{ref}}=0.5$. At this reference speed, compressibility effects are present, but shock waves do not appear at the nose-cylinder junction. The relevant Reynolds number based on the main cylinder diameter $U_e d/\nu$ is $5\times10^6$. The inviscid flow pressure distributions were computed using the code developed by Keller and South.[27] The boundary-layer calculations were carried out using these inviscid pressure distributions. There are two potentially troublesome regions of pressure gradient: one is the strong adverse pressure gradient near the forebody/concave junction; the other is the strong acceleration followed by an adverse pressure gradient region at the main cylinder shoulder. Calculations showed that in the worst case the former leads to separation and the latter to the formation of shock waves and/or separation. The location of separation (zero wall shear) is marked in Figs. 12 and 13. A parametric study was then conducted to essentially control the pressure gradient in these two regions.

In the present work, the surface tangents are matched at the curvature junctions. The nose-body dimensions are nondimentionalized by the main cylinder diameter $d$: the parameters studied for the nose body shown in Fig. 12 are forebody diameter and length, ratio of concave to convex radii of curvature, and concave/convex match point location (defined by the turning angle $\phi$), which determines the lengths of the curved regions. Figure 12 shows changes in pressure distribution due to changes in the parameters of the curvature, keeping the forebody unchanged. However, none of these geometries could prevent separation near the flat/concave junction without a passive bleed.

Changes in the length of the forebody did not prevent separation either. To alleviate the adverse pressure gradients, the forebody was slightly flared (5 deg). The pressure distributions of the nose bodies with this additional parameter are shown in Fig. 13. Although the adverse pressure gradient was reduced by the flare, it was still not adequate to prevent separation.

There are several ways of alleviating this boundary-layer separation. One is by the so-called inverse design approach of, for example, Zedan and Dalton.[28] According to that approach, a desirable pressure distribution, i.e., likely to prevent separation, should first be chosen from experience. In Figs. 12 and 13, such a distribution could be obtained by smoothing the dip in the neighborhood of separation. Then the body geometry that would create such a distribution could be computed back. Boundary-layer computations can then be carried out to check if separation has indeed been prevented. However, this approach has not been taken here, speculating that it is likely to redefine the geometry substantially in a way that separation will be prevented, but the essential geometric features like $\delta/R$ and $\Delta s/\delta_i$ of convex curvature and other viscous drag reduction concepts, which are the main thrust of the present work, are likely to get obscured in the process. (In hindsight, there is a need to explore if the inverse approach can prevent separation, while leaving undisturbed the parameters of the convex curvature concept of viscous drag reduction.) An alternative that could prevent separation while preserving the present drag reduction concepts is a passive bleed from the concave region of the single-stage bodies to the downstream flat shoulder region of the main cylinder[4]. A further advantage of this will be an added reduction in wall shear stress levels in the upstream region of the main cylinder due to injection. However, the above two approaches were not followed here and, instead, a rather different conservative passive approach was taken. This is given in the following.

### C. Distribution of Area Ratio

As both Figs. 12 and 13 show, in the above two generic bodies substantial changes in the geometrical parameters produced only marginal changes in the pressure field. This can be understood by plotting the axial variation of the cross-sectional area ratio. This is shown in Fig. 14. Figure 14 (a and b) shows that in the first two generic bodies, the increase in area ratio essentially takes place rather abruptly. Thus, since the pressure field due to the large area ratio segments basically "overwhelms" that due to the small area ratio segments,

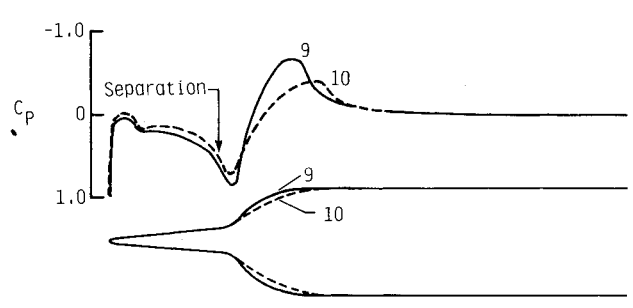


**Fig. 13 Computed surface-pressure distributions in single-stage nose geometries with mildly flared forebodies. Computed separation location in both geometries is indicated, $M_{\text{ref}}=0.5$.**

changes in the latter have very little effect on the overall pressure field.

The aforementioned suggests that for the present purpose, the area ratio is to be distributed more gradually than that in Fig. 14 (a and b). Figure 14c is an example of such a desirable distribution, and it is considered in the following.

### D. Three-Stage Nose Body

Figure 14c shows the gradual nature of the distribution of area ratio in a typical three-stage nose body. The diameter ratio of the forecylinder is much larger now. This is because the "concept" is being applied over only three stages. In principle, more stages can be incorporated. The computations were carried out for a main cylinder diameter of 18 in., but the results are given in a nondimensional form.

The three-stage nose body (geometry No. 13) and its surface pressure distribution are shown in Fig. 15, and the corresponding wall shear stress distribution, considering all effects, is shown in Fig. 16. The boundary-layer computation now indicated no separation, although the $\delta/R$ values for this body are only between 0.5–1%—far less than the minimum 5% level required for optimization. The definition of geometry No. 13 is as follows: nose ellipse $b/a = 0.2$, $2R/d = 0.6$ in all concave and convex surface, $\phi = 20$ deg in each concave and convex turn, diameter ratio is 0.4, 0.6, and 0.8 in the three forecylinders, and the length of each forecylinder is $0.4a$. In Fig. 16 the wall shear stress distribution of the three-stage nose-body combination has been compared with that of two equivalent nose bodies having conventional half-elliptic cross sections. These equivalent noses are defined based on surface area and volume. A half-elliptic nose having a $b/a$ of 0.2234 has the same volume as the three-stage nose. A half-elliptic nose having a $b/a$ of 0.1722 has the same surface area as the three-stage nose. The ratio of the three-stage nose area to the equivalent-volume nose area is 1.29, and the ratio of the three-stage nose volume to the volume of the equivalent-area nose is 0.78. The equivalent-area and equivalent-volume noses are 74 and 58% of the axial length of the three-stage nose, respectively. A detailed comparison of the integrated viscous drag levels of the three nose body combinations (Fig. 16) is given in Sec. IV.

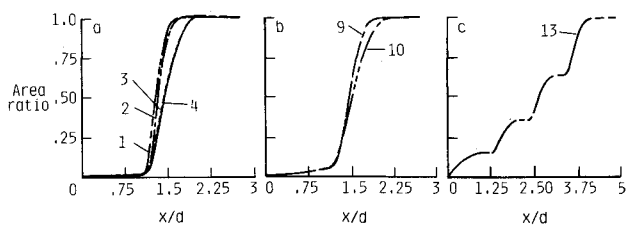


**Fig. 14 Axial variation of cross-sectional area ratio in the single- (a) and (b), and three-stage nose bodies (c). The geometry identification numbers are indicated. The forebody cylinder is straight in (a), but mildly flared in (b).**

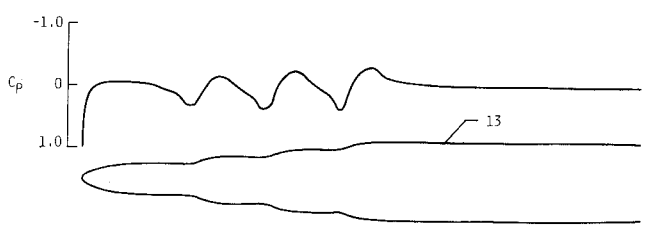


**Fig. 15 Computed surface pressure distributions in the three-stage nose body (geometry No. 13). Note absence of separation, $M_{ref} = 0.5$.**

### E. Indirect Verification of the Computational Design

A direct experimental verification of the computed pressure and wall shear stress distributions shown in Figs. 15 and 16, respectively, is required before the estimated viscous drag reduction breakdowns of the nose and the main cylinder presented in the next section can be considered firmly established. That is a substantial task and is beyond the scope of this paper. However, an indirect verification of the computational design has been carried out, and this is described in the following.

After the work described thus far was completed, Mr. D. M. Bushnell brought the author's attention to the measurements of Smits and Joubert.[25] A relevant candidate of computation is their Lucy Ashton body of revolution, which resembles the three-stage body in several ways. The curved flow computations described in the first part of this paper are largely concerned with two-dimensional geometries—the only geometry that is axisymmetric is that of Smits et al.[24] Such data are rare because most curved boundary-layer experiments are being conducted in two-dimensional and not axisymmetric geometries. Apparently, the reason why experimentalists have been overoccupied with two-dimensional geometries is their desire to study the curvature effect in the absence of other complicating extra strain rates like longitudinal pressure gradients, lateral divergence, and transverse curvature. Therefore, it was decided to compute the Lucy Ashton boundary layer using exactly the same codes as used for the three-stage bodies. The computed inviscid pressure distribution is compared against the faired measurements in Fig. 17. This computed pressure distribution was then used for boundary-layer computations. The computed skin-friction and momentum-thickness distributions are compared against measurements in Fig. 18. It is very encouraging to see that the agreement is quite satisfactory. Since no constant was adjusted for this flow, the computations can indeed be deemed a prediction rather than a postdiction. Note that skin-friction and other boundary-layer characteristics have been uniformly computed well in the two axisymmetric bodies (Figs. 11 and 18). On the other hand, the agreement in $H$ and $Re_\theta$ in the two-dimensional geometries is not uniformly that good. It is suspected that this is due to the following aspects of the two-dimensional experiments. Commonly, the pressure gradient and boundary-layer history in the precurvature flat regions have not been documented by the experimenters, making the task of matching the computation and measurements at the first station difficult. The test surface flow is intimately associated with that in the remaining walls due to the presence of a three-dimensional pressure

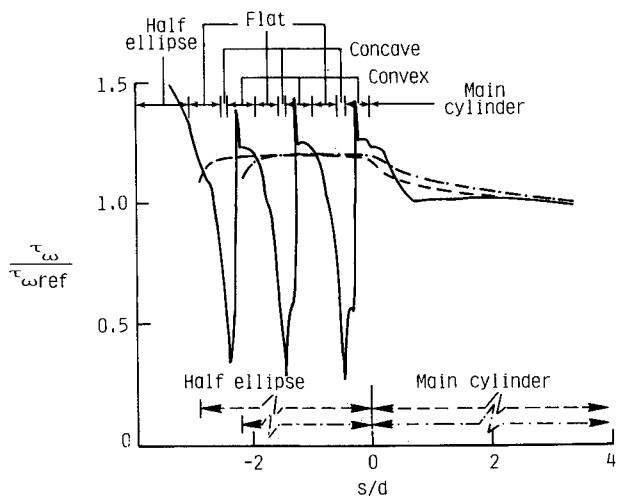


**Fig. 16 Computed wall shear stress distributions in three-stage nose body (No. 13) (solid line) compared with equivalent-area (dashed line) and equivalent-volume (chain line) half-elliptic noses, $M_{ref} = 0.5$, $\tau_{wref} = 4.566 \times 10^{-3}$ psi.**

field[9]—a feature that is usually ignored in two-dimensional computations. On the other hand, the axisymmetric bodies do not have any such flow-controlling nontest surfaces.

In summary, it is noted that the two axisymmetric boundary layers[24,25] computed successfully have most of the features of the three-stage body. These features are longitudinal concave and convex surface curvatures, lateral divergence, transverse surface curvatures, and alternating longitudinal wall static-pressure gradients. Identical laminar-to-turbulent transition specification has been prescribed in all axisymmetric flow computations presented in this paper. The only important effect that is not simultaneously present in the two axisymmetric bodies of Smits and co-workers[24,25] is compressibility which, in any case, is expected to have a beneficial effect. Therefore, in the above computation a state-of-the-art verification of the computational design, although in an indirect manner, has been made.

## IV. Discussion

To highlight the effect of relaxation over the main cylinder, the friction drag is estimated from the computed wall-shear stress distributions in two stages. First, the drag acting up to the intersection of the most downstream part of the noses with the main cylinder, called the shoulder, is considered. Then, the relaxation over the main cylinder is also included to obtain the total friction drag. In the following, the relaxation over the main cylinder is considered up to an $s/d$ of about 3.0.

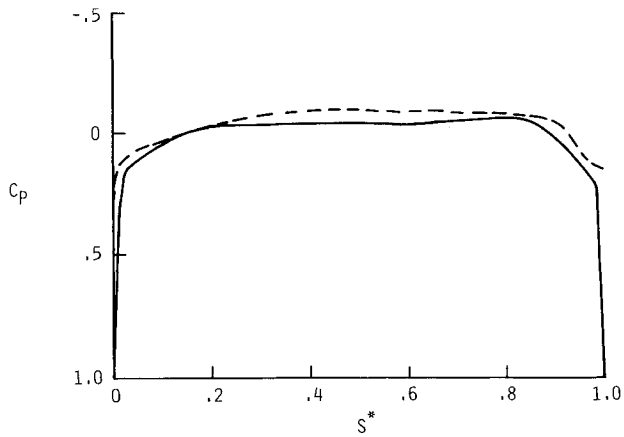


**Fig. 17 Computed surface pressure distributions compared with measurements[25] in Lucy Ashton body of revolution. Solid line—computations; broken—faired line through measurements, $U_{ref}$ = 21.5 m/s.**

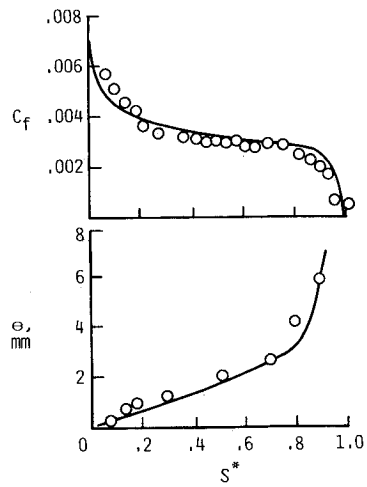


**Fig. 18 Computations compared with measurements[25] in Lucy Ashton body of revolution. Experimental $H$ not given, $U_{ref}$ = 21.5 m/s.**

When computed from the nose tip to the shoulder only, the three-stage nose-friction drag is about 14.8% less than that in the equivalent-area half-elliptic nose, and it is about 7.7% lower when the main cylinder is also included (the normalizing drag is higher in the latter case). Note that a lower viscous drag in the three-stage nose-body combination means a lower momentum thickness at the tail of the main cylinder, which in turn implies a thinner wake. To take into account the difference in volume between the three-stage nose and the equivalent-area nose, a reduced surface area $A$ can be defined as $A = V^{2/3}$, where $V$ is volume. When viewed this way, up to the shoulder, the three-stage nose viscous $C_d$ turns out to be 1.9% higher than that in the equivalent-area nose. However, when the main cylinder is also taken into account, the three-stage viscous $C_d$ becomes lower by about 1.6%, which, of course, is rather small.

A similar comparison has also been made between the three-stage and the equivalent-volume half-elliptic noses. Up to the shoulder, the three-stage nose-friction drag is higher by 9.3%, and it is higher by only 1.2% when the relaxation over the main cylinder is also taken into account. The relative wall-shear stress levels in Fig. 16 suggest a break-even of the viscous drag at a slightly higher $s/d$ than considered here.

Presently, there is no pressure and boundary-layer data available on the kind of multistage nose-body combinations presented here, and experiments are clearly needed to verify their viscous drag reduction potential. Such data will also be a new test bed for turbulence models.

In the above nose-body computations, the viscous-inviscid interaction was ignored based on the assumption that the concept was being applied in the nose area where the boundary-layer displacement effect was small. The satisfactory agreement between measurements and computations shown in Figs. 17 and 18 indirectly showed this to be justified. Nevertheless, a direct check was made, and the nose bodies were also computed by a viscous-inviscid method.[29] (Mr. L. M. Putnam is thanked for introducing the author to this aspect of the study). There, a relaxation solution of the full potential-flow equations was iteratively combined with an integral solution of the boundary-layer equations. The viscous drag coefficients of the three nose-body combinations, with and without the main cylinders, were compared as before. This interactive method showed an identical trend in the viscous drag difference of the three-stage nose body with respect to the two equivalent nose bodies as given in the previous two paragraphs. This check confirmed that the viscous-inviscid interaction is negligible in the present study.

In the present work, the emphasis has been on the reduction of the viscous component of drag. Unlike other contemporary viscous drag reduction approaches,[4,14] the definition of a net drag reduction here is not a straightforward matter because of the simultaneous changes in several variables like surface area, volume, frontal area, axial distributions of cross-sectional area, weight, and overall length between competing noses. In other words, the present drag reduction approach has a "systems" nature. In addition, since the bodies are not closed, the pressure and total drag values cannot be determined.

## V. Concluding Remarks

In this paper, useful evaluation of a mixing-length model in turbulent boundary layers over curved surfaces has been given. It is concluded that the convex curvature concept of viscous drag reduction can be applied to an axisymmetric nose body in a passive manner without causing any separation if the application is made in multiple stages of short regions of curvature. However, the concept could only be applied at a level far below the optimum, and improvements may be possible.

Recent experimental research on curved and other complex turbulent boundary layers has revealed several interesting behaviors that have a viscous drag reduction potential. These

results remain unutilized and scattered in the literature. The present work has attempted to apply them in a coherent manner.

## Acknowledgment

Helpful discussions with Mr. D. M. Bushnell and Professor V. C. Patel are gratefully acknowledged. The former has also reviewed an earlier version of the paper. Support of this work by NASA (NAS1-18235) is acknowledged.

## References

[1]Smits, A. J., Young, S. T. B., and Bradshaw, P., "The Effect of Short Regions of High Surface Curvature on Turbulent Boundary-Layers," *Journal of Fluid Mechanics,* Vol. 94, Pt. 2., Sept. 1979, pp. 209–242.

[2]Gillis, J. C. and Johnston, J. P., "Turbulent Boundary-Layer Flow and Structure on a Convex Wall and its Redevelopment on a Flat Wall," *Journal of Fluid Mechanics,* Vol. 135, Oct. 1983, pp. 123–153.

[3]Alving, A. E. and Smits, A. J., "The Recovery of a Turbulent Boundary Layer from Longitudinal Curvature," AIAA Paper 86-0435, Jan. 1986.

[4]Bushnell, D. M., "Turbulent Drag Reduction for External Flows," AIAA Paper 83-0227, Jan. 1983.

[5]Bradshaw, P., "Effects of Streamline Curvature on Turbulent Flow," AGARD AG-169, Aug. 1973.

[6]Saffman, P. G., "Problems and Progress in the Theory of Turbulence," *Structure and Mechanisms of Turbulence II,* edited by H. Fiedler, *Lecture Notes in Physics,* No. 76, Springer-Verlag, Berlin, 1977, pp. 273–306.

[7]Galbraith, R. A. McD. and Head, M. R., "Eddy Viscosity and Mixing Length from Measured Boundary-Layer Developments," *Aeronautics Quarterly,* Vol. 26, May 1975, pp. 133–154.

[8]Schlichting, H., *Boundary-Layer Theory,* 7th ed., McGraw-Hill, New York, 1979, p. 583.

[9]Patel, V. C. and Richmond, M. C., "Pressure Gradient and Surface Curvature Effects in Turbulent Boundary Layers," AIAA Paper 87-1301, June 1987.

[10]Adams, E. W. and Johnston, J. P., "A Mixing-Length Model for the Prediction of Convex Curvature Effects on Turbulent Boundary Layers," *Transactions of the ASME Journal of Fluid Engineering,* Vol. 106, Jan. 1984, pp. 142–148.

[11]Moser, R. D. and Moin, P., "The Effects of Curvature in Wall-Bounded Turbulent Flows," *Journal of Fluid Mechanics,* Vol. 175, Feb. 1987, pp. 479–510.

[12]Cary, A. M., Weinstein, L. M., and Bushnell, D. M., "Drag-Reduction Characteristics of Small Amplitude Rigid Surface Waves," *Progress in Astronautics and Aeronautics: Viscous Flow Drag-Reduction,* Vol. 72, edited by G. R. Hough, AIAA, New York, 1980, pp. 144–167.

[13]Harris, J. E. and Blanchard, D. K., "Computer Program for Solving Laminar, Transitional, or Turbulent Compressible Boundary-Layer Equations for Two-Dimensional and Axisymmetric Flow," NASA TM 83207, Feb. 1982.

[14]Bandyopadhyay, P. R., "Review—Mean Flow in Turbulent Boundary Layers Disturbed to Alter Skin Friction," *Transactions of the ASME Journal of Fluid Engineering,* Vol. 108, June 1986, pp. 127–140.

[15]Eidson, T., "Drag-Reduction Report: Micro Air Bearings and Convex Curvature," NASA CR NAS1-16096, Feb. 1984.

[16]Simon, T. W., Moffat, R. J., Johnston, J. P., and Kays, W. M., "Turbulent Boundary-Layer Heat Transfer Experiments: Convex Curvature Effects Including Introduction and Recovery," NASA CR-3510, Feb. 1982.

[17]Muck, K. C., Hoffmann, P. H., and Bradshaw, P., "The Effect of Convex Surface Curvature on Turbulent Boundary Layers," *Journal of Fluid Mechanics,* Vol. 161, Dec. 1985, pp. 347–369.

[18]Youssefmir, P., "Flow Structure of Full-Coverage Film Cooling on a Convexly Curved Surface," Engineering Thesis, Stanford Univ., Stanford, CA, 1982.

[19]So, R. M. C. and Mellor, G. L., "An Experimental Investigation of Turbulent Boundary Layers Along Curved Surfaces," NASA CR-1940, April 1972.

[20]Shizawa, T. and Honami, S., "Experiment on Turbulent Boundary Layers Over a Concave Surface—Effects of Introduction of Curvature," *Proceedings of the Fourth Symposium on Turbulent Shear Flows,* Univ. of Karlsruhe, Karlsruhe, FRG, 1983, pp. 6.38–6.43.

[21]Hoffmann, P. H., Muck, K. C., and Bradshaw, P., "The Effect of Concave Surface Curvature on Turbulent Boundary Layers," *Journal of Fluid Mechanics,* Vol. 161, Dec. 1985, pp. 371–403.

[22]Hoffmann, P. H. and Bradshaw, P., "Turbulent Boundary Layers on Surfaces of Mild Longitudinal Curvature," Imperial College, Aeronautical Rept. 78-04, 1978.

[23]Taylor, M. and Smits, A. J., "The Effects of a Short Region of Concave Curvature on a Supersonic Turbulent Boundary Layer," AIAA Paper 84-0169, Jan. 1984.

[24]Smits, A. J., Eaton, J. A., and Bradshaw, P., "The Response of a Turbulent Boundary Layer to Lateral Divergence," *Journal of Fluid Mechanics,* Vol. 94, Pt. 2, Sept. 1979, pp. 243–268.

[25]Smits, A. J. and Joubert, P. N., "Turbulent Boundary Layers on Bodies of Revolution," *Journal of Ship Research,* Vol. 26, June 1982, pp. 135–147.

[26]Smits, A. J., "The Control of Turbulent Boundary Layers by the Application of Extra Strain Rates," AIAA Paper 85-0538, March 1985.

[27]Keller, J. P. and South, J. C., Jr., "RAXBOD—A FORTRAN Program for Inviscid Transonic Flow Over Axisymmetric Bodies," NASA TM X-72831, Feb. 1976.

[28]Zedan, M. F. and Dalton, C., "The Inverse Method Applied to a Body of Revolution with an Extended Favorable Pressure Gradient Forebody," *Communications of Applied Numerical Methods,* Vol. 2, 1986, p. 113.

[29]Wilmoth, R. G., "RAXJET: A Computer Program for Predicting Transonic, Axisymmetric Flow Over Nozzle Afterbodies with Supersonic Jet Exhausts," NASA TM 83235, Feb. 1982.